

Experimental evidence for topological phases in the magnetoconductance of 2DEG-based hybrid junctions

Kaveh Delfanazari^{1,2,3,*}, Llorenç Serra⁴, Pengcheng Ma², Reuben K. Puddy², Teng Yi², Moda Cao², Yilmaz Gul², Ian Farrer^{2,5}, David A. Ritchie², Hannah J. Joyce¹, Michael J. Kelly^{1,2}, Charles G. Smith²

¹Electrical Engineering Division, Engineering Department, University of Cambridge, Cambridge CB3 0FA, UK

²Department of Physics, Cavendish Laboratory, University of Cambridge, Cambridge CB3 0HE, UK

³James Watt School of Engineering, University of Glasgow, Glasgow G12 8QQ, UK

⁴IFISC (UIB-CSIC) and Physics Department, University of the Balearic Islands, E-07122 Palma, Spain

⁵Department of Electronic and Electrical Engineering, University of Sheffield, Mappin Street, Sheffield, S1 3JD, UK

*Corresponding author email: kd398@cam.ac.uk

Dated: 25062020

Several theoretical studies have recently predicted that the Majorana phases could be realized as quantized plateaus in the magnetoconductance of the artificially engineered hybrid junctions based on two-dimensional electron gases (2DEG) under fully *out-of-plane* magnetic fields¹⁻⁵. The large transverse Rashba spin-orbit interaction in 2DEG together with a strong orbital effect due to magnetic fields yield topological phase transitions to nontrivial phases hosting Majorana modes. Such Majorana modes are formed at the ends of 2DEG-based wires with a hybrid superconductor-semiconductor integrity. Here, we report on the experimental observation of such topological phases in hybrid junctions on an In_{0.75}Ga_{0.25}As 2DEG platform by sweeping small *out-of-plane* magnetic fields ($B_{\perp} < 100$ mT) and probing the conductance to highlight the characteristic quantized magnetoconductance plateaus. The observed signature of topological phases in small out-of-plane magnetic fields in planar hybrid junctions suggests that In_{0.75}Ga_{0.25}As heterostructure affords a promising material platform for the realization of scalable topological circuits for the applications in quantum technologies.

Topological superconductors with a superconducting gap in their bulk and topologically protected metallic states on their edges and surfaces host exotic quasiparticles such as anyons and Majorana fermions. Such exotic (non-abelian) quasiparticles have been proposed for manipulation and application in fault-tolerant topological quantum processing and computing because their quantum states defined by a pair of Majorana zero modes (MZMs) work as a nonlocal qubit [1-18]. Therefore, the search effort for the realization of topological superconductors, in both artificial and intrinsic forms, has been considerably increased recently.

Artificially engineered topological superconductors in hybrid superconductor-semiconductor (S-Sm) material platforms have attracted substantial attention because they offer stimulating opportunities to create and manipulate non-Abelian MZMs [10-13]. The charge-less zero-bias peak (ZBP) in the differential conductance of the S-Sm structures above a high critical in-plane magnetic field (usually ≥ 0.5 T) has been shown to be the signature of topological phases in hybrid devices [6,8,17,18]. However, the application of a relatively large in-plane magnetic field to achieve the required phase transitions makes such a system unfeasible in many applications. Therefore, a different approach towards the realization of artificial topological superconductors is sought [1-5,7,19,20].

Here, we report on the first experimental observation of topological superconductivity in hybrid junctions, on a two-dimensional electron gas (2DEG) platform, in a fully perpendicular (out-of-plane) magnetic field. We show that transitions to topological phases can be observed as signatures in the junctions' magnetoconductance. We furthermore demonstrate that such phases can be tuned with very small, out-of-plane magnetic fields. Our observation is based on the recent theoretical proposal for the existence of topological phases in the magnetoconductance of hybrid junctions based on a 2DEG coupled to superconducting contacts [1]. The single (NS) and double (NSN) hybrid junctions reveal topological phase transitions to nontrivial phases as a consequence of an

enhanced magneto orbital effect, due to applied external magnetic fields, and in the presence of strong transverse Rashba spin-orbit (SO) interaction in a 2DEG. Such junctions host Majorana modes in their hybrid segment. The presence of a potential barrier at the junction interface reveals the Majorana phases as quantized plateaus of high conductance for narrow junctions. In wider junctions, where the SO interaction becomes stronger relative to the transverse confinement, the sequence of multiple transitions trivial-topological- trivial, and so on, takes place at low fields with characteristic magnetoconductance features. The conductance yields quantized plateaus in the topological phases with a Majorana mode, while it is quenched in the trivial regions. These differences are caused by the presence of an interface barrier that strongly suppresses the Andreev reflection [21] and reduces the conductance of the trivial regions.

On the contrary, the Majorana state of the nontrivial regions allows maintaining a high conductance even in the presence of an interface barrier. Therefore, the influence of the interface barrier in trivial and topological regions is very different. Importantly, the quenched conductance of the trivial regions causes a dip in conductance, followed by an enhancement when the field is such that a nontrivial phase is entered.

Figure 1 (a) shows the schematic view of the studied Josephson junctions in the presence of an out-of-plane magnetic field. The superconducting Nb leads (grey parts on two sides of the device) act on the piece of the 2DEG beneath and between them to form the hybrid 2DEG (red regions) by the proximity effect. The quantum transport then occurs between the top Nb (grey)- hybrid 2DEG (red)- normal 2DEG (black)- hybrid 2DEG (red)- bottom Nb (grey) in the presence of out-of-plane magnetic fields, see Fig. 1 (a).

Note that when the vertical field is switched off, the normal 2DEG (black) no longer exists between two Nb pads and the device gets the form of Nb- hybrid 2DEG-Nb Josephson junction because the Andreev reflections in such ballistic junctions carry supercurrent in the normal 2DEG part (see temperature/magnetic

field dependent supercurrent data in SI). Figure 1 (b-c) is the result of a theoretical model for our Josephson junctions with two superconducting contacts based on Ref. [1] for an illustrative case. The phase boundaries in the μ - B plane correspond to the condition of a $k = 0$ propagating mode at zero energy of the hybrid junction. That is the $k = 0$ gap-closing lines in the μ - B plane. Figure 1 (b) shows the phase boundaries for a junction of width $w = 1 \mu\text{m}$. Note that there are many boundaries packed at low field. If one increases the field along the cyan dotted lines, the topological junction changes phase as 0- 1- 0- 1... Majorana modes each time a topological phase line is crossed. That is, the junction is evolving along the sequence of trivial- topological- trivial- topological... phases [1]. As the field is increased, the number of propagating modes of the normal section decreases. For instance, along the cyan dotted lines of Fig. 1 (b), the evolution each time a line is crossed is N - $(N-1)$ - $(N- 2)$ - ... , with N being the number of modes at zero fields. The Andreev reflection is perfect for all channels when the topological section is in a Majorana mode phase, and that is imperfect in phases with no Majorana modes. The Andreev reflection of the trivial phases decreases quadratically as the field is increased from the initial value of that phase.

Figure 1 (c) shows the modeled conductance for the field sequence along three-dotted cyan lines in the left panel (Fig. 1b). Note that the quadratic decrease of the trivial phases leads to dips before the onset of the next phase. These dips are especially apparent for the initial transitions where the number of propagating modes is higher. All three conductance curves show flat quantized plateaus in steps of around $2e^2/h$. The schematic side view of the studied 2D junctions is shown in Fig. 1 (d). The devices are fabricated by contacting Nb (shown in grey) to 30 nm thick high-quality $\text{In}_{0.75}\text{Ga}_{0.25}\text{As}$ two-dimensional electron gas that is formed 120 nm below the surface of an $\text{In}_{0.75}\text{Al}_{0.25}\text{As}/\text{GaAs}$ heterostructure wafer [23-26]. Figure 1 (e) is the scanning electron micrograph (SEM) of the quantum chip with an array of 2D junctions, eight independently controlled Josephson junctions on this chip. In our CAD design, two Nb leads of width $w = 4 \mu\text{m}$ are

separated with a length $L = 850$ nm through $\text{In}_{0.75}\text{Ga}_{0.25}\text{As}$ quantum wells. However, these dimensions are subject to change after fabrication by wet-etching technique and especially under the application of vertical fields, as we explain below [23]. The SEM of one junction is shown in Fig. 1 (f). The motivation behind our approach with quantum integrated circuits includes fabricating and measuring an array of devices in one fridge cool-down with minimum experimental condition variations. From an array of eight devices on a single chip, one failed during the fabrication process. We observed quantum transport in three devices, but with weaker induced superconductivity and high field conductance structures- they will be discussed in detail elsewhere.

The other four devices show strongly induced superconductivity, multiple Andreev reflections, and large supercurrent of up to $2 \mu\text{A}$ [see SI file]. These junctions are named as D1-4 and discussed in full detail in this paper. The elastic mean free path of these junctions is around $l_e = e^{-1} \hbar \mu_e \sqrt{2\pi n_s} \cong 2 \mu\text{m}$ thus all junctions are in the ballistic regime [23] and the coherence length of around $2 \mu\text{m}$ in 2DEG calculated from Equation $\xi_N = \hbar v_{\text{FN}} / \pi \Delta_{\text{Nb}}$ suggest that they are in a short junction limit, too [23]. An average normal state resistance of $R_N = 0.2 \text{ k}\Omega$ is also measured in these junctions.

Figure 2 (a) shows the quantized conductance observation as a function of the out-of-plane magnetic field for D1 measured at $T = 50$ mK and 620 mK. It shows the magnetic field sweep for two different directions: the red and orange curves show a sweep from $+0.4$ T to -0.4 T. In contrast, the blue and dark green curves show the reversed sweep from -0.4 T to $+0.4$ T. By increasing field from 0 T to ± 0.4 T, the conductance drops and quantized plateaus appear when the magnetic field is between 0 and ± 0.08 T, and the base temperatures range is between $T = 50$ mK and 320 mK. Figure 2 (b) is a close look of Fig. 2 (a) at small magnetic field ranges to highlight the plateaus for both directions of magnetic fields. By reversing fields from ± 0.4 T to 0 T, the conductance of the junction increases.

Between $B = \pm 0.08$ T and 0 T (see Figs 2 (a-d)), the conductance plateaus are again observed for temperatures below $T = 320$ mK. The plateaus are slightly different for two magnetic field sweep directions: from -0.08 T to 0 T and from 0 T to +0.08 T, as shown in Fig. 2 (e) and (f), respectively. We believe that the difference might be due to the occurrence of bunching of transitions in low fields, and we may only probe one feature due to experimental resolution limitation. The heating effects in the device for two negative/positive magnetic field sweep directions might also affect the conductance plateaus. We can see that the conductance plateaus with quantized values in steps of around $2 e^2/h$ observed in the experiment are in excellent agreement with our model which predicts a roughly similar amount of transport modes with quantized conductance in hybrid 2D junctions (see Fig. 1 c and the discussion in materials and methods section about the model).

The conductance curve at $T = 50$ mK shows a sequence of low field phase transitions on the junction conductance. It suggests that a scattering barrier may be formed at the interface of the junction that strongly quenches the conductance of the trivial phases, causing a dip in the conductance curve. In contrast, the conductance remains quantized in topological ones due to the enhanced Andreev reflection. To further investigate the origin of the observed conductance plateaus, we look at the effect of the temperature and magnetic field sweep rate. The quantized conductance at temperatures between $T = 50$ mK and 320 mK for magnetic fields between $-0.08 < B$ (T) < 0 and magnetic fields between $0 < B$ (T) $< +0.08$ branches of G for field sweeps from -0.4 T to +0.4 T are replotted in Figs. 2 (e) and 2 (f), respectively. The corresponding number of plateaus as a function of magnetic field and temperature is shown in Fig. 3 (a).

We observe five plateaus at the lowest base temperature ($T = 50$ mK) in which this number decreases as temperature increases, due to the reduction in the Andreev reflection probabilities. Still, their positions (plateaus steps) are almost unchanged. Figure 3 (b) shows the quantized conductance for D2 observed for

reversed applied magnetic fields ranging of $0 < B_{\perp}$ (mT) $< +80$ at $T= 50$ mK at different field sweep rates: 0.1 T/hrs (orange), 0.2 T/hrs (blue), 0.5 T/hrs (red) and 1 T/hrs (black). As can be inferred from this figure, the number of plateaus and their widths do not change, which suggests that the phase transition is also independent of the field sweep rate.

Figure 4 shows the normalized conductance as a function of the applied out-of-plane field at temperature $T= 50$ mK for D3 at 1st run for sweep direction from left to right (a), 2nd run for sweep direction from right to left (b), 3rd and 4th runs for sweep direction from left to right (c) and right to left (d). Looking at Fig. 4, it is remarkable that the conductance of the hybrid junction in trivial phases is quenched by showing robust dips, but it is unaffected in topological regions.

Figure 5 shows quantized plateaus for D4 measured at temperatures $T= 50$ mK (a), 120 mK (b), 220 mK (c), and 320 mK (d), for a narrower range of magnetic fields with sweep direction from +0.4 T to 0 T. Here, we highlight the observed quantized plateaus with apparent dips that are a manifestation of the topological phase transitions of the hybrid junction. All our investigations show that the conductance plateaus observation is quite robust and reproducible in different devices at different temperatures, magnetic field sweeps rates, and also magnetic field sweep directions. There are small variations in the dip and peak positions of the plateaus of different devices. They may be explained in a way that the effective dimensions of the junctions after fabrication, by a wet etching method, might differ from the design values giving rise to a different number of active modes in the junctions, thus affecting their conductance.

From the given values of $R_N \approx 0.2$ k Ω , electron density n_s , mobility μ_e and interface transparency of our high-quality Nb-In_{0.75}Ga_{0.25}As-Nb junctions [23] we can estimate the number of modes to be around $N \cong 100$ in a junction with designed width $w= 4$ μm [18]. However, our junctions are made by the wet-etch technique, so the effective dimension of the junctions would normally be subject to changes after fabrication and this can be estimated from the number of modes

in the conductance of the junctions [17,18]. From the conductance of our devices in the experiment, we can infer the number of transport modes to be roughly $50 \leq N \leq 80$. This fits roughly in a junction width of around $0.8 \leq w \text{ (}\mu\text{m)} \leq 2$. By looking at our calculated conductance in Fig. S5, Fig. 1, and Fig. S6 for Josephson junctions of widths $w = 0.75 \text{ }\mu\text{m}$, $1 \text{ }\mu\text{m}$, and $1.25 \text{ }\mu\text{m}$, respectively, we find a good agreement between experiment and theory both in the number of modes and also in the observed quantized conductance plateaus with the steps of roughly around $2 e^2/h$. A similar change in the effective dimensions of Josephson junctions was also reported quite widely in Josephson junctions of different material systems, for instance, in 2DEG [18, 29] as well as in nanowire [30].

From data shown in Figs. 2 (a), in addition to the plateaus observation, it is also found that the conductance curve peaks *asymmetrically* near $B = 0$, and hysteresis is observed when the applied fields are reversely swept. We attribute this effect to the small magnetic impurity in the chip. Semiconducting wafers with a significantly reduced number of defects, and therefore with high electron mobility, can be produced by the molecular beam epitaxy, but the defects cannot be completely avoided in the device. The other possible source of impurity might be the evaporation/sputtering chambers where the ohmic contacts and Nb films have been deposited/sputtered [23,27]. Therefore, the internal effective magnetic field B_{eff} may slightly differ [28] from the applied external out-of-plane field B_{\perp} due to magnetic interactions in our devices and the observation of asymmetric conductance with a hysteresis (see Fig. S7 and its corresponding explanation for more detail).

In short, we presented the evidence for topological phases in the magnetoconductance of hybrid junctions in a scalable quantum circuitry under a fully vertical (out-of-plane) magnetic field. Our experimental results are consistent with the topological phase transitions in the 2D material system in small out-of-plane magnetic fields. We introduced a radically different but quite

efficient and robust approach towards topological phase detection in planar Josephson junctions. We demonstrated that array of topological junctions could be integrated on a single chip so one can fabricate array and network of 2D topological junctions on a single chip for various purposes such as for braiding the Majoranas or measuring/assessing their reproducibility, quantum yield, and reliability for their use in quantum technologies in one fridge cool-down with minimum experimental ambient condition variations. Our approach may also help the development of robust quantum integrated circuitry for applications in decoherence-free quantum computation and secure communication.

Materials and Methods

The $\text{In}_{0.75}\text{GaAs}/\text{In}_{0.75}\text{AlAs}/\text{GaAs}$ quantum well was grown by molecular beam epitaxy (MBE)^{23-26, 31}. The 30 nm thick 2DEG InGaAs quantum well with density $n_s=2.24\times 10^{11}$ (cm^{-2}) and mobility $\mu_e=2.5\times 10^5$ (cm^2/Vs) in the dark was formed 120 nm below the wafer surface. The fabrication methods of various types of 2D Josephson junctions on a semiconducting chip have been extensively discussed in our previous works [23-26]. Here, we bring a summary:

Using photolithography and wet etching, in which a sulfuric acid solution of compositions H_2SO_4 , H_2O_2 , and H_2O were used, we created an active region (a raised area referred to as mesa structure and shown by two parallel dashed line in Fig. 1 e) with length $l' = 1440$ μm and $w' = 160$ μm in the middle of our chip where all the eight identical junctions are patterned and fabricated (see Fig. 1). To make junctions, after photolithography patterning, we removed the top InGaAs and InAlAs layers in the patterned area using wet etching. The etch produces a 120–140 nm deep trench in this area, which is around the 120 nm depth of the $\text{In}_{0.75}\text{Ga}_{0.25}\text{As}$ quantum well. This was followed by the deposition of a ≈ 130 nm Nb film (about three times larger than the London penetration depth of Nb, which is 40 nm) to make high-quality superconducting contacts to the 2DEG, using DC

magnetron sputtering in an Ar plasma. According to the design, each junction has a length of $L = 850$ nm at the shortest path, which increases to $26\text{ }\mu\text{m}$ at the edge of the active region and a width of $w = 4\text{ }\mu\text{m}$ as shown in Figure 1. The ohmic contacts were made of gold/germanium/nickel (AuGeNi) to get a low resistance and good chemical bond (adhesion) to the semiconductor substrate and placed $100\text{ }\mu\text{m}$ away from two Nb– $\text{In}_{0.75}\text{Ga}_{0.25}\text{As}$ quantum well interfaces to reduce any influence of the normal electrons on the interface. Not all of the ohmic pads were used for source-drain bias measurements in this study. Gold wire of diameter $20\text{ }\mu\text{m}$ were used for the bond wires. The quantum transport measurements of conductance as a function of temperature and magnetic fields were performed by using a standard lock-in technique by superimposing a small ac-signal at a frequency of 70 Hz and an amplitude of $5\text{ }\mu\text{V}$ to the junction dc bias voltage and measuring the ac-current.

Numerical modeling:

Our model is based on the recent theoretical proposal on evidence for Majorana phases in the magnetoconductance of topological junctions based on 2DEGs [1]. A model Hamiltonian of a hybrid junction with a width w , where $-w/2 < y < w/2$, can be written as

$$H = \left(\frac{p_x^2 + p_y^2}{2m} - \mu \right) \tau_z + \frac{\alpha}{\hbar} (p_x \sigma_y - p_y \sigma_x) \tau_z + \Delta_B \sigma_z + \Delta_0 \tau_x + \frac{\hbar^2}{2ml_z^4} y^2 \tau_z - \frac{\hbar}{ml_z^2} y p_x - \frac{\alpha}{l_z^2} y \sigma_z, \quad (1)$$

Here, α , Δ_B , Δ_0 , μ , m , and σ (τ) is the SO interaction, Zeeman, pairing parameters, chemical potential, effective mass, and Pauli matrices in spin (particle-hole) space, respectively. The Zeeman energy Δ_B is related to the field B by $\Delta_B = g^* \mu_B B / 2$ with $g^* = 15$ as the gyromagnetic factor. The other parameters of the model are induced superconductivity $\Delta_0 = 60\text{ }\mu\text{eV}$ (close to $\Delta_0 \cong 100\text{ }\mu\text{eV}$ observed

in the experiment for most junctions fabricated in our group [23]), the strength of the Rashba spin-orbit interaction $\alpha = 20 \text{ meVnm}$ [18], and $m = 0.039 m_e$ [31].

The orbital field terms, the last three terms in Equation (1), are related to the magnetic length $l_z^{-2} = eB/\hbar c$. We highlight here that the last three terms in Equation (1) are often neglected in studies of Majorana modes in hybrid junctions of almost 1D wires. By performing the microscopic modeling of narrow 2D single SN junctions, the conductance G can be calculated from [1]

$$G = \frac{e^2}{h} (N - R + R_A) \quad (2)$$

and in a double NSN junction, in the same way, the conductance gets the form of

$$G = \frac{e^2}{h} (T + R_A) \quad (3)$$

where, N , R , R_A , and T are the number of incident electron modes, normal reflection probability, Andreev reflection probability, and transmission from the left to right normal contact, respectively.

When the junction width increases, the microscopic solution of the scattering problem, especially for SNS double junctions, becomes complicated. The difficulties stem from a large number of modes within a reduced energy interval and to the strong fluctuations with the magnetic field. However, Hoppe *et. al* demonstrated that the conductance of a long SNS double junction G_{SNS} is given by the Andreev reflection R_A of a single SN junction so that the SNS junction conductance can be written as $G_{\text{SNS}} = R_A e^2/h$ [22]. In phenomenological modeling based on Ref. [1], the magnetoconductance $G(B)$ of an SNS junction for fields $B \in [B_1, B_2]$ can be written as

$$G(B) = \frac{e^2}{h} \begin{cases} N_i & \text{if topological} \\ N_i \left[1 - \gamma \left(\frac{B - B_1}{B_2 - B_1} \right)^2 \right] & \text{if trivial} \end{cases} \quad (4)$$

where, B_1 and B_2 indicate initial and final fields of a given phase of the hybrid S-Sm 2DEG strip, γ is a phenomenological parameter and N_i is the number of incident electronic modes from the normal side of the junction. As anticipated

[1], a perfect Andreev reflection in topological phases is assumed and a parabolic decrease in trivial phases.

References

1. L. Serra and K. Delfanazari, Evidence for Majorana phases in the magnetoconductance of topological junctions based on two-dimensional electron gases, *Phys. Rev. B* **101**, 115409 (2020).
2. M. P. Nowak and P. Wójcik, Renormalization of the Majorana bound state decay length in a perpendicular magnetic field, *Phys. Rev. B* **97**, 045419 (2018).
3. P. Wójcik and M. P. Nowak, Durability of the superconducting gap in Majorana nanowires under orbital effects of a magnetic field, *Phys. Rev. B* **97**, 235445 (2018).
4. B. Nijholt and A. R. Akhmerov, Orbital effect of magnetic field on the Majorana phase diagram, *Phys. Rev. B* **93**, 235434 (2016).
5. J. Osca and L. Serra, Majorana states and magnetic orbital motion in planar hybrid nanowires, *Phys. Rev. B* **91**, 235417 (2015).
6. V. Mourik *et al.*, Signatures of Majorana fermions in hybrid superconductor-semiconductor nanowire devices. *Science* **336**, 1003–1007 (2012).
7. L. P. Rokhinson, X. Liu, J. K. Furdyna, The fractional a.c. Josephson effect in a semiconductor-superconductor nanowire as a signature of Majorana particles. *Nat. Phys.* **8**, 795–799 (2012).
8. M. T. Deng, *et al.*, Majorana bound state in a coupled quantum-dot hybrid-nanowire system. *Science* **354**, 1557–1562 (2016).
9. A. Das, Y. Ronen, Y. Most, Y. Oreg, M. Heiblum, H. Shtrikman, Zero-bias peaks and splitting in an Al–InAs nanowire topological superconductor as a signature of Majorana fermions, *Nat. Phys.* **8**, 887–895 (2012).
10. E. Majorana, A symmetric theory of electrons and positrons. *Soryushiron Kenkyu* (Engl. transl.) **63**, 149 (1981).
11. A. Yu. Kitaev, Unpaired Majorana fermions in quantum wires. *Phys. Usp.* **44**, 131 (2001).
12. J. D. Sau, R. M. Lutchyn, S. Tewari, S. Das Sarma, Generic new platform for topological quantum computation using semiconductor heterostructures. *Phys. Rev. Lett.* **104**, 040502 (2010).

13. J. Alicea, Majorana fermions in a tunable semiconductor device. *Phys. Rev. B* **81**, 125318 (2010).
14. R. M. Lutchyn, J. D. Sau, S. Das Sarma, Majorana fermions and a topological phase transition in semiconductor-superconductor heterostructures. *Phys. Rev. Lett.* **105**, 077001 (2010).
15. Y. Oreg, G. Refael, F. von Oppen, Helical liquids and Majorana bound states in quantum wires. *Phys. Rev. Lett.* **105**, 177002 (2010).
16. F. Pientka, A. Keselman, E. Berg, A. Yacoby, A. Stern, B. I. Halperin, Topological Superconductivity in a Planar Josephson Junction, *Phys. Rev. X* **7**, 021032 (2017).
17. A. Fornieri, A. M. Whiticar, F. Setiawan, E. P. Martin, A. C. C. Drachmann, A. Keselman, S. Gronin, C. Thomas, T. Wang, R. Kallagher, G. C. Gardner, E. Berg, M.J. Manfra, A. Stern, C. M. Marcus, and F. Nichele, Evidence of topological superconductivity in planar Josephson junctions, *Nature* **569**, 89–92 (2019).
18. H. Ren, F. Pientka, S. Hart, A. Pierce, M. Kosowsky, L. Lunczer, R. Schlereth, B. Scharf, E. M. Hankiewicz, L. W. Molenkamp, B. I. Halperin, and A. Yacoby, Topological Superconductivity in a Phase-Controlled Josephson Junction, *Nature* **569**, 93–98 (2019).
19. J. Osca and L. Serra, Majorana states and magnetic orbital motion in planar hybrid nanowires, *Phys. Rev. B* **91**, 235417 (2015).
20. J. Osca, L. Serra, Topological suppression of magnetoconductance oscillations in normal–superconductor junctions, *Phys. Status Solidi B* **254**, 1700135 (2017). Complex band-structure analysis and topological physics of Majorana nanowires, *Eur. Phys. J. B* **92**, 101 (2019).
21. A. F. Andreev, Thermal conductivity of the intermediate state of superconductors. *Sov. Phys. JETP.* **19**: 1228 (1964).
22. H. Hoppe, U. Zülicke, G. Schön, Andreev reflection in strong magnetic fields, *Phys. Rev. Lett.* **84**, 1804 (2000).
23. K. Delfanazari, R. K. Puddy, P. Ma, T. Yi, M. Cao, Y. Gul, I. Farrer, D. A. Ritchie, H. J. Joyce, M. J. Kelly, C. G. Smith, On-Chip Andreev Devices: hard Gap and Quantum Transport in Ballistic Nb-In_{0.75}Ga_{0.25}As quantum well-Nb Josephson junctions, *Adv. Mater.* **29**, 1701836 (2017).
24. K. Delfanazari, R. K. Puddy, P. Ma, T. Yi, M. Cao, Y. Gul, I. Farrer, D. A. Ritchie, H. J. Joyce, M. J. Kelly, C. G. Smith, Proximity induced superconductivity in indium gallium arsenide quantum wells, *J. Magn. Magn. Mater.* **459**, 282 (2018).

25. K. Delfanazari, R. K. Puddy, P. Ma, T. Yi, M. Cao, C. Richardson, I. Farrer, D. A. Ritchie, H. J. Joyce, M. J. Kelly, C. G. Smith, On-chip hybrid superconducting-semiconducting quantum circuit, *IEEE Trans. Appl. Supercond.* **28**, 1100304 (2018).
26. K. Delfanazari, R. K. Puddy, P. Ma, T. Yi, M. Cao, Y. Gul, C. Richardson, I. Farrer, D. A. Ritchie, H. J. Joyce, M. J. Kelly, C. G. Smith, Scalable quantum integrated circuits on superconducting two-dimensional electron gas platform, *J. Vis. Exp.* in press (2019).
27. D. Maryenko, A. S. Mishchenko, M. S. Bahramy, A. Ernst, J. Falson, Y. Kozuka, A. Tsukazaki, N. Nagaosa, M. Kawasaki, Observation of anomalous Hall effect in a non-magnetic two-dimensional electron system, *Nat. Communications* **8**, 14777 (2017).
28. S. Vaitiek'enas, Y. Liu, P. Krogstrup, C. M. Marcus, Zero-field Topological Superconductivity in Ferromagnetic Hybrid Nanowires, *arXiv: 2004.02226v1* (2020).
29. Z. Wan, A. Kazakov, M. J. Manfra, L. N. Pfeiffer, K. W. West, L. P. Rokhinson, *Nat. Commun.* **6**, 7426 (2015).
30. J. Paajaste, M. Amado, S. Roddaro, F. S. Bergeret, D. Ercolani, L. Sorba, F. Giazotto, *Nano Lett.* **15**, 1803 (2015).
31. C. Chen, I. Farrer, S. N. Holmes, F. Sfigakis, M. P. Fletcher, H. E. Beere, D. A. Ritchie, *J. Cryst. Growth* **425**, 70 (2015).

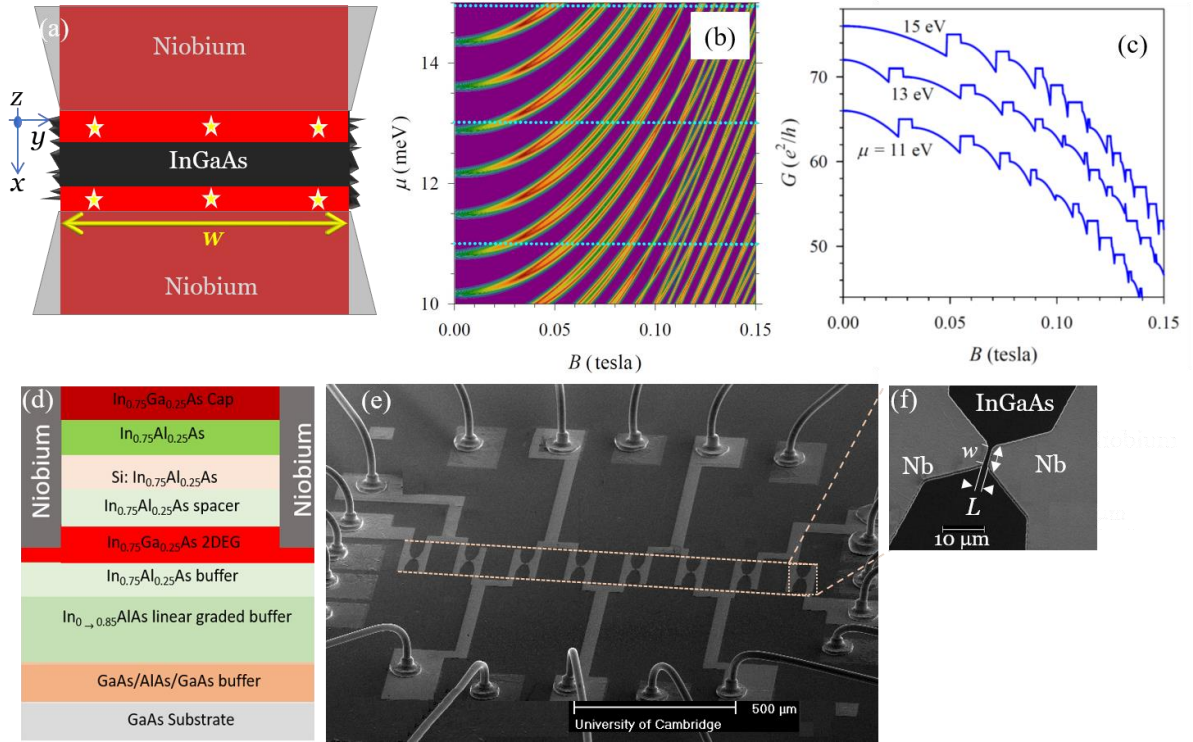


Figure 1. Topological phases in hybrid Josephson junctions: (a) A schematic view of a hybrid Josephson junction, under vertical magnetic fields. The superconducting Nb leads (grey parts) act on the piece of the 2DEG beneath and between them to form the hybrid 2DEG (red parts) by the proximity effect. The quantum transport proceeds between the top Nb (grey)- hybrid 2DEG (red)-normal 2DEG (black)- hybrid 2DEG (red)- bottom Nb (grey) in the presence of vertical magnetic fields. Stars are the boundary between normal and hybrid 2DEGs where Majorana modes are expected. Note that when the vertical field is switched off, the normal 2DEG (black) no longer exists between two Nb pads and the device gets the form of Nb- hybrid 2DEG-Nb Josephson junction because the Andreev reflections in the ballistic junctions carry supercurrent in the normal 2DEG part (see text and SI figures). (b) Phase diagram of the hybrid 2DEG (red in Fig. 1a) showing the boundaries between trivial (magenta) and topological regions with width $w = 1 \mu\text{m}$, a value close to the effective width of the junction in the experiment. The phase boundaries of the diagram have been calculated as the $k = 0$ gap closings. We consider superconductivity $\Delta_0 = 60 \mu\text{eV}$ in hybrid 2DEG which is close to the induced gap value observed in experiment. (c) Theoretical conductance of the junction taking the sequence of magnetic fields for three line cuts as cyan dotted lines in panel (b). The model assumes a perfect Andreev reflection in the topological phases (plateaus), and a decreasing Andreev reflection AR (dips) with increasing field in the trivial phases due to interface scattering. (d) The schematic view of an In_{0.75}Ga_{0.25}As/In_{0.75}Al_{0.25}As/GaAs heterostructure. Superconducting Nb leads are attached to high quality In_{0.75}Ga_{0.25}As quantum wells to form hybrid 2DEG by proximity induced superconductivity. (e) Scanning electron microscope image of the hybrid quantum circuit with an array of 2D symmetric and planar junctions on a chip. The superconducting parts are niobium (Nb) and shown in grey. The ohmic contacts are etched down to 2DEG region, for the purpose of tunneling measurements between Nb and 2DEG. The area between Nb and ohmic pads are all etched away except the active area (mesa shown with two parallel dashed-brown lines) where Josephson junctions are formed (dashed-brown square for one junction). (f) An SEM image of one junction on the chip.

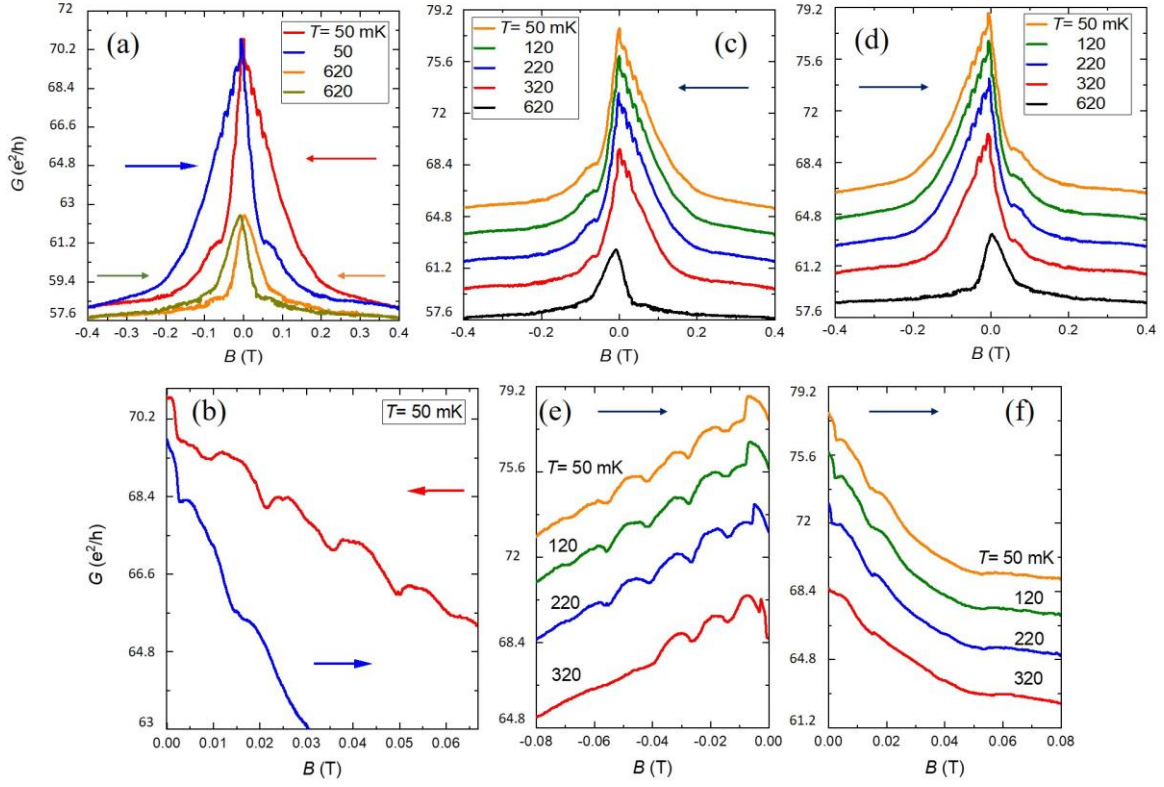


Figure 2. **Temperature dependence of the quantized conductance in topological Josephson junction:** (a) conductance vs. applied out-of-plane magnetic field B_{\perp} , at $V_{SD}=0$ and at different base temperatures, for D1. (b) same information for a smaller range of magnetic fields to highlight that the quantized plateaus are observed in both directions. quantized conductance for magnetic field B_{\perp} sweep directions from +0.4 T to -0.4 T (c) and from -0.4 T to +0.4 T (d). Strong asymmetric conductance G curves are observed. (e)-(f) data shown in (d) are replotted for narrower magnetic field B_{\perp} ranges to highlight the plateaus. The plateaus are a bit broadened for the increasing fields (possibly due to coincidence of bunch of transitions at low B_{\perp} (as predicted in the model) and one has been probed in the experiment). (e) all curves in Figs. (c)-(f) are shifted vertically by $0.9 e^2/h$ for clarity.

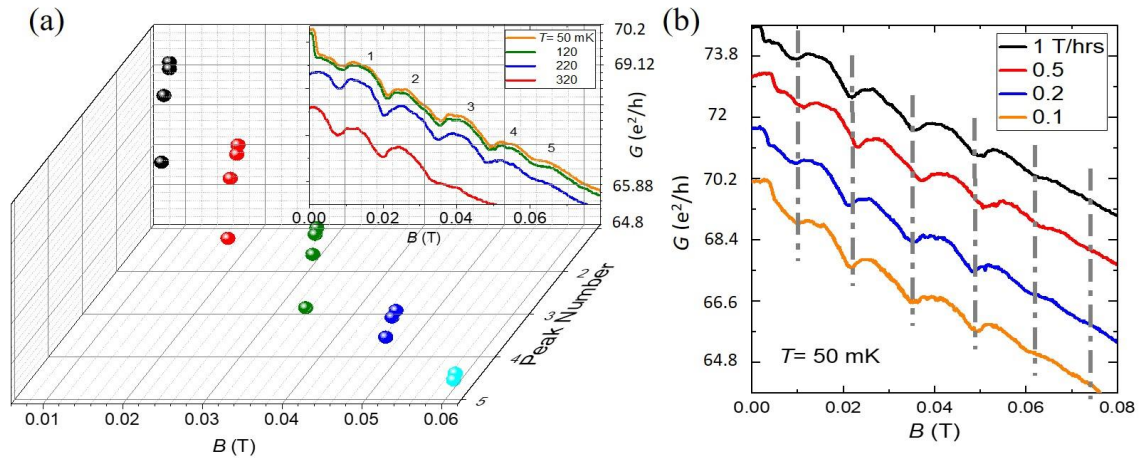


Figure 3. **Temperature and magnetic field sweep rate dependences of the quantized conductance in topological Josephson junctions:** (a) plateaus observed in D1 are numbered (inset) and plotted as a function of temperature and magnetic field B_{\perp} . (b) quantized conductance observed for reversed applied magnetic fields ranging of $0 < B_{\perp}$ (mT) < 80 at $T = 50$ mK, at different field sweep rates: 0.1 T/hrs (orange), 0.2 T/hrs (blue), 0.5 T/hrs (red) and 1 T/hrs (black), for D2. The curves are vertically shifted by $0.54 e^2/h$ for clarity. The plateaus are quite robust and the number of plateaus and their step sizes remain nearly unchanged under different magnetic field sweep rates.

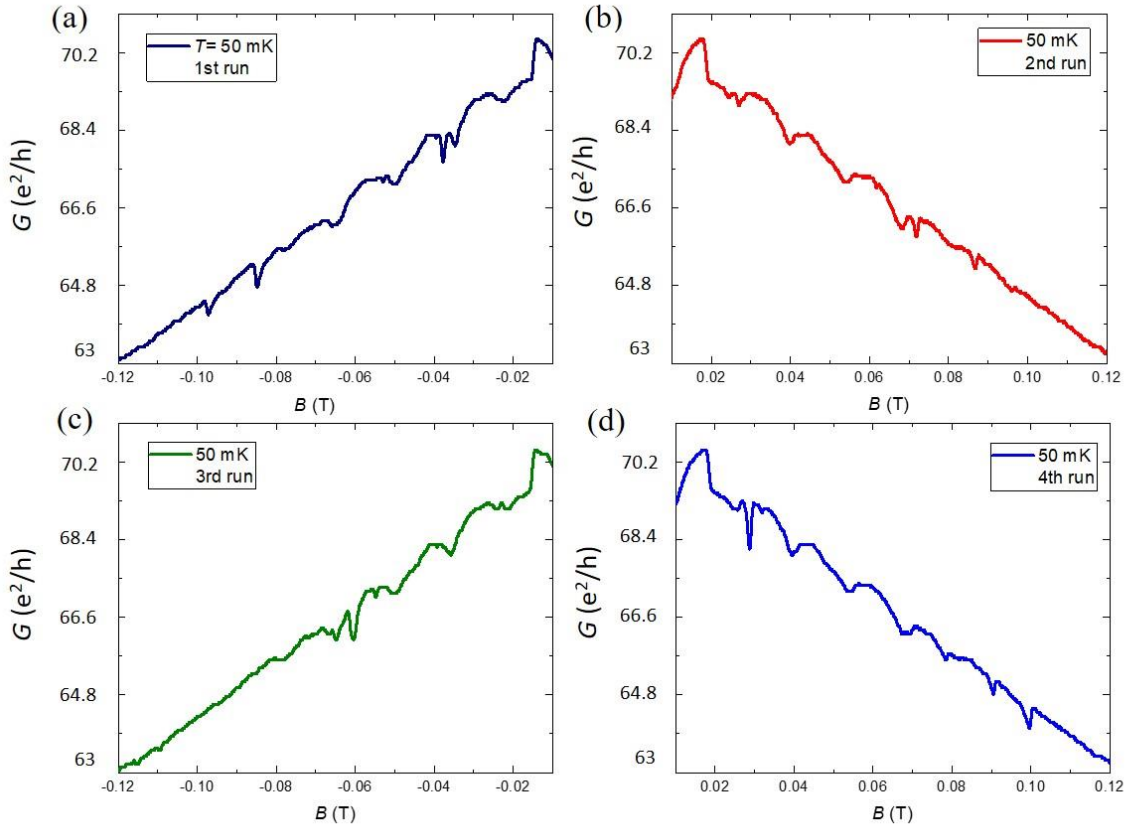


Figure 4. Reproducibility of the quantized conductance in topological Josephson junctions at different sweep directions: the quantized conductance as a function of applied out-of-plane magnetic field B_{\perp} for D3 at 1st (a) and 3rd (c) runs with sweep direction from left to right and, 2nd (b) and 4th (d) runs with sweep direction from right to left. All data are taken at temperature $T=50$ mK. The quantized plateaus and phase transitions are quite robust and reproducible at different magnetic field sweep directions.

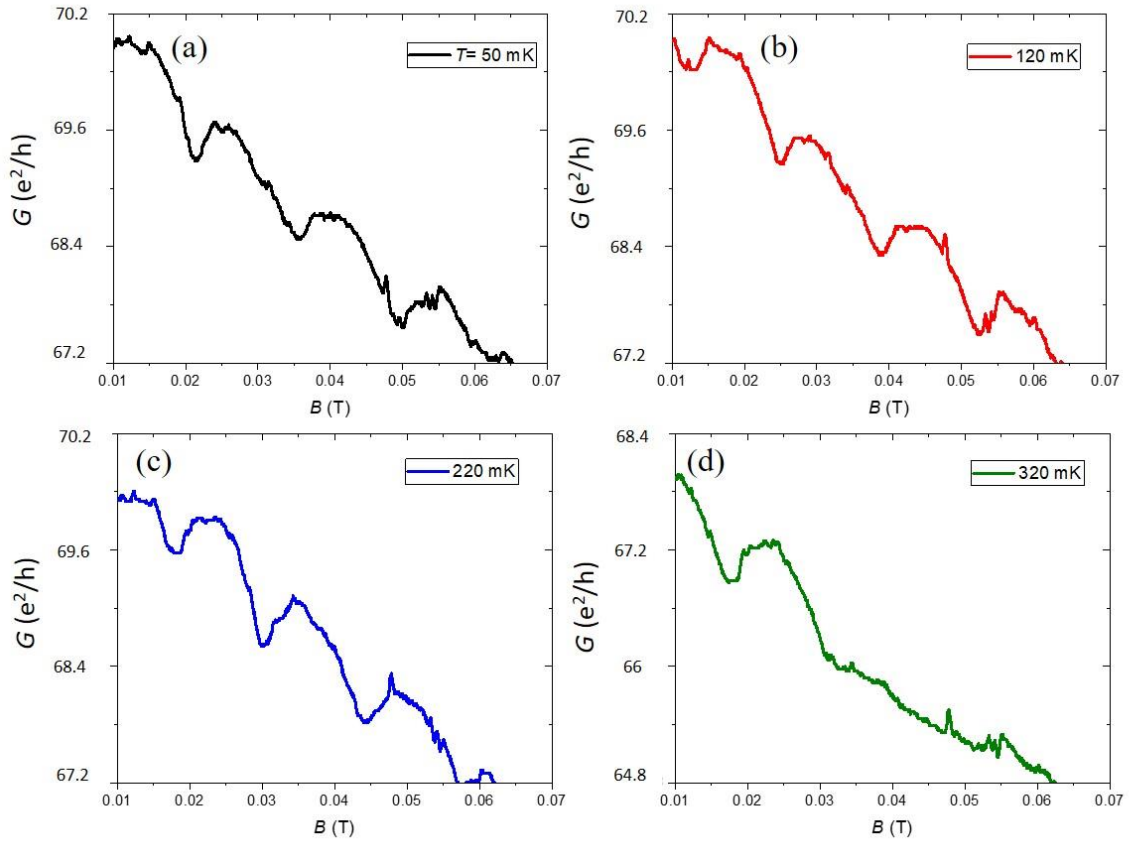


Figure 5. **Temperature dependence of the quantized conductance in topological Josephson junctions:** quantized conductance vs. applied out-of-plane field B_{\perp} at temperatures $T= 50$ mK (a), $T= 120$ mK (b), $T= 220$ mK (c), and $T= 320$ mK (d), for fields sweep directions from right to left, for D4. The curves are plotted for a selected (small) range of magnetic fields to highlight the robustness of the plateaus and phase transitions.

SUPPLEMENTARY INFORMATION

Experimental evidence for topological phases in the magnetoconductance of 2DEG-based hybrid junctions

Kaveh Delfanazari^{1,2,3,*}, Llorenç Serra⁴, Pengcheng Ma², Reuben K. Puddy², Teng Yi², Moda Cao², Yilmaz Gul², Ian Farrer^{2,5}, David A. Ritchie², Hannah J. Joyce¹, Michael J. Kelly^{1,2}, Charles G. Smith²

¹Electrical Engineering Division, Engineering Department, University of Cambridge, Cambridge CB3 0FA, UK

²Department of Physics, Cavendish Laboratory, University of Cambridge, Cambridge CB3 0HE, UK

³James Watt School of Engineering, University of Glasgow, Glasgow G12 8QQ, UK

⁴IFISC (UIB-CSIC) and Physics Department, University of the Balearic Islands, E-07122 Palma, Spain

⁵Department of Electronic and Electrical Engineering, University of Sheffield, Mappin Street, Sheffield, S1 3JD, UK

[*Corresponding author email: kd398@cam.ac.uk](mailto:kd398@cam.ac.uk)

Dated: 25062020

Here, we demonstrate the quantum transport in hybrid junctions measured at sub-Kelvin temperature ranges and/or under vertical magnetic fields [1].

Figure S1 shows the induced superconductivity in $\text{In}_{0.75}\text{Ga}_{0.25}\text{As}$ for four devices (D1-4). All data are taken at $T = 50$ mK. An excess current I_{exc} flows through the junctions as a result of electron- and hole-like quasiparticles correlations (Andreev reflections) below the junctions' transition temperatures and for voltage biases within the superconducting gap. The dV/dI (V_{SD}) value is reduced in the gap region [2-4], and supercurrents with critical currents of up to 2 μA are measured [1].

Figure S2 shows the temperature dependence induced superconductivity and supercurrent in $\text{In}_{0.75}\text{Ga}_{0.25}\text{As}$ quantum wells. The dV/dI (V_{SD}) curves for temperatures between $T = 50$ mK and 800 mK for D4 are plotted in Fig. S2 (a). We observed a flat dV/dI (V_{SD}) within Δ/e with subharmonic gap structures (SGS), suggesting highly transparent interfaces between two different materials based on Blonder–Tinkham–Klapwijk (BTK) theory [1,5]. The barrier strength is estimated to be $Z < 0.2$ (Z is the dimensionless interface barrier strength) in the

interfaces between Nb and $\text{In}_{0.75}\text{Ga}_{0.25}\text{As}$, and the induced gap of approximately $100 \leq \Delta_{\text{ind}} (\mu\text{eV}) \leq 300$ is measured in D1-4 [1]. The temperature and source-drain voltage dependences induced superconducting gap with pronounced SGS peaks and dips for D4 are shown in Fig. S2 (b). The multiple Andreev reflections (MAR) at the interfaces of the Nb- $\text{In}_{0.75}\text{Ga}_{0.25}\text{As}$ -Nb junctions result in the observation of SGS in the differential conductance. At the lowest measured temperature $T = 50$ mK, the SGS appears with three peaks (named as P1, P2, and P3 in Fig. S2 (a)) and three dips (named as d1, d2, and d3 in Fig. S2 (a)). The temperature evolution of the peaks and dips due to the suppression of the induced superconductivity with temperature increase can be seen here. The SGS peak positions obey the expression $V = 2\Delta/ne$ (Δ is the Nb gap energy, $n = 1, 2, 3, \dots$ is an integer, and e is the electron charge) [1]. All features are significantly temperature-dependent, and the strongest (weakest) SGS peaks (dips) are observed at $T = 50$ mK (800 mK). The shape of the gap and SGS has been shown to be influenced by the ratio of L/ξ_N where ξ_N is the Bardeen–Cooper–Schrieffer coherence length [5-7]. The SGS consists of a set of pronounced maxima in dV/dI at $V = 2\Delta/ne$ if $L/\xi_N \ll 1$, but the amplitude of the SGS decreases by increasing the ratio of L/ξ_N . For $L \approx \xi_N$ the peaks evolve into dips [7,8]. Both the induced gap and SGS are suppressed significantly at temperatures above $T = 400$ mK leading to a shift toward zero bias as shown in Fig. S2 (b). The current–voltage characteristics (IVC) at various temperatures is plotted in Fig. S2 (c). A pronounced supercurrent is observed in this high quality Nb- $\text{In}_{0.75}\text{Ga}_{0.25}\text{As}$ -Nb junction at zero magnetic fields and low temperatures between $T = 50$ and 500 mK.

The magnetic field dependence of the induced superconductivity is shown in Fig. S3 for device 4. The color-coded plot of dV/dI as a function of applied perpendicular magnetic field B_{\perp} and applied voltage V_{SD} , at $T = 50$ mK, is shown in Fig. S3 (a). It can be seen that the induced gap and SGS features that are

evidence of enhanced multiple Andreev reflections in high-quality Josephson junctions are quite sensitive to the applied external field. Both effects are suppressed; the position of the peaks shifts toward zero bias, and their amplitudes diminish with further increasing of the magnetic field. Figure S3 (b) shows that the induced superconductivity and SGS are strongly B_{\perp} dependent, with the position of the peaks bending toward zero voltage as B_{\perp} is increased. The dark yellow, blue, and dark cyan triangles (see their corresponding arrows in inset) indicate the magnetic field evolution of the induced and SGSs. The plot of dV/dI as a function of applied voltage V_{SD} at $B_{\perp} = 1$ mT is shown in the inset, demonstrating a robust induced superconducting gap and SGSs in the high-quality Josephson junction.

On our ballistic junctions, the coherent Andreev reflections and correlation of electrons and holes lead to bound states and, therefore, the phase-coherent supercurrents between the electrodes. Figure S4 (a) shows the IVC at the lowest and highest measured temperatures for D3 in the inset. The largest critical current I_c was measured at the lowest temperature of $T = 50$ mK. I_c is suppressed as the temperature increases and disappeared above $T = 350$ mK, as shown by dark cyan triangles. The magnetic field dependence of the induced superconductivity is shown in Fig. S4 (b) and (c) for D3. The applied perpendicular fields affect the phase of the induced superconductivity in the 2DEG that is confined between Nb superconducting electrodes. As a result, the I_c would oscillate, and the period of $I_c(B)$ would change continuously and nonmonotonically from Φ_0 to $2\Phi_0$, where $\Phi_0 = h/2e$ is the flux quantum (Fraunhofer-like) [1,7-9]. However, both trivial [7-9] and topological [10-12] Josephson junctions can reveal widely different oscillation patterns, strongly depending on their topology, dimensions, and material characteristics. For example, I_c in trivial junctions does not decrease to zero if the 2DEG is not enclosed between superconducting contacts [7], or may get a different period due to the change in the effective dimension of junctions

[9]. Topological junctions, due to Majorana modes, may show a pattern with a nonzero first minimum, deviating from a standard Fraunhofer pattern [10], or may show a suppression of the odd-numbered lobes in the Fraunhofer pattern [11], or may reveal smaller-than expected flux periods ΔB [12].

In our junctions, 2DEG is not fully enclosed between two Nb contacts [1,7]. We observe the oscillation of I_c , usually with flux periods of around $\Delta B \cong 0.8$ mT [1]. This is approximately corresponding to an area of $A \cong \Delta\Phi/\Delta B \cong 2.5 \mu\text{m}^2$ of 2DEG sandwiched between two Nb electrodes which are slightly smaller than the area of the 2DEG between Nb electrodes at the closest path, which should be $\cong 3 \mu\text{m}^2$ based on the CAD design [1]. In the presence of the vertical magnetic field, we, therefore, estimate that effective dimension of the junctions are slightly changed [1,7-12] and their width w and length L may get the sizes between $0.8 \leq w (\mu\text{m}) \leq 2$ and $2 \leq L (\mu\text{m}) \leq 1$ taking in to account the coherence length of $\approx 2 \mu\text{m}$ in 2DEG in our ballistic and highly coupled junctions [1]. This would result in the number of transport modes between $60 \leq N \leq 80$ in the conductance of the junctions [13] and is in a good agreement with the conductance of the junctions calculated based on our model and also measured in the experiment.

Figures **S5** and **S6** are the theoretical modeling based on the approach of [14] for a narrower ($w= 0.75 \mu\text{m}$) and wider ($w= 1.25 \mu\text{m}$) Josephson junction, respectively, as compared to the $1 \mu\text{m}$ wide junction shown in the main text (Fig.1 b-c). It is clearly seen how for wider junctions, the topological phases are more densely packed in the μ - B plane and how this leads to a sequence of very closely spaced conductance dips and plateaus as a function of the magnetic field. We note that already for $w= 1.25 \mu\text{m}$ resolving the sequence of such transitions with increasing fields requires an extremely fine magnetic sweep, at the limit of the numerical possibility and well beyond the experimental one.

Figure S7 (a) shows a phenomenological curve for a hysteretic $B_{\text{eff}}(B)$ similar to Ref [15], although with much smaller internal field enhancements. We assume that the switching field B_s is very close to zero, and it signals the position of a sudden jump in B_{eff} due to a large reorientation of the internal magnetization. Figure S7 (b) shows that the phenomenological magnetoconductance Equation (4), see Materials and Methods, when presented as $G(B_{\text{eff}}(B))$, qualitatively reproduces the experimental hysteresis between forward and backward sweeps of the magnetic field [15]. This phenomenological model, including internal magnetic interactions, agrees with the experiment about the presence of a sequence of conductance dips at a rather low field as well as the presence of the hysteresis.

References:

1. K. Delfanazari, R. K. Puddy, P. Ma, T. Yi, M. Cao, Y. Gul, I. Farrer, D. A. Ritchie, H. J. Joyce, M. J. Kelly, C. G. Smith, *Adv. Mater.* **29**, 1701836 (2017).
2. L. Aggarwal, A. Gaurav, G. S. Thakur, Z. Haque, A. K. Ganguli, G. Sheet, *Nat. Materials* **15**, 32–37 (2016).
3. H. B. Heersche, P. Jarillo-Herrero, J. B. Oostinga, L. M. K. Vandersypen, Alberto F. Morpurgo, *Nature* **446**, 56–59 (2007).
4. P. Samuelsson, Å. Ingeman, G. Johansson, E. V. Bezuglyi, V. S. Shumeiko, G. Wendin, R. Kürsten, A. Richter, T. Matsuyama, U. Merkt, *Phys. Rev. B* **70**, 212505 (2004).
5. G. E. Blonder, M. Tinkham, T. M. Klapwijk, *Phys. Rev. B* **25**, 4515 (1982).
6. J. C. Cuevas, J. Hammer, J. Kopu, J. K. Viljas, M. Eschrig, *Phys. Rev. B* **73**, 184505 (2006).
7. Z. Wan, A. Kazakov, M. J. Manfra, L. N. Pfeiffer, K. W. West, L. P. Rokhinson, *Nat. Commun.* **6**, 7426 (2015).
8. H. Y. Günel, N. Borgwardt, I. E. Batov, H. Hardtdegen, K. Sladek, G. Panaitov, D. Grützmacher, and Th. Schapers, *Nano Lett.* **14**, 4977–4981 (2014).
9. J. Paajaste, M. Amado, S. Roddaro, F. S. Bergeret, D. Ercolani, L. Sorba, F. Giazotto, *Nano Lett.* **15**, 1803 (2015).

10. Potter, A. C.; Fu, L. *Phys. Rev. B*, **88**, 121109 (2013).
11. Baxevanis, B.; Ostroukh, V. P.; Beenakker, C. W. J. *Phys. Rev. B*, **91**, 041409 (2015).
12. Williams, J. R.; Bestwick, A. J.; Gallagher, P.; Hong, S. S.; Cui, Y.; Bleich, A. S.; Analytis, J. G.; Fisher, I. R.; Goldhaber-Gordon, *Phys. Rev. Lett.* **109**, 56803 (2012).
13. H. Ren, F. Pientka, S. Hart, A. Pierce, M. Kosowsky, L. Lunczer, R. Schlereth, B. Scharf, E. M. Hankiewicz, L. W. Molenkamp, B. I. Halperin, and A. Yacoby, *Nature* **569**, 93–98 (2019).
14. L. Serra and K. Delfanazari, Evidence for Majorana phases in the magnetoconductance of topological junctions based on two-dimensional electron gases, *Phys. Rev. B* **101**, 115409 (2020).
15. S. Vaitiek'enas, Y. Liu, P. Krogstrup, C. M. Marcus, *arXiv*: 2004.02226v1 (2020).

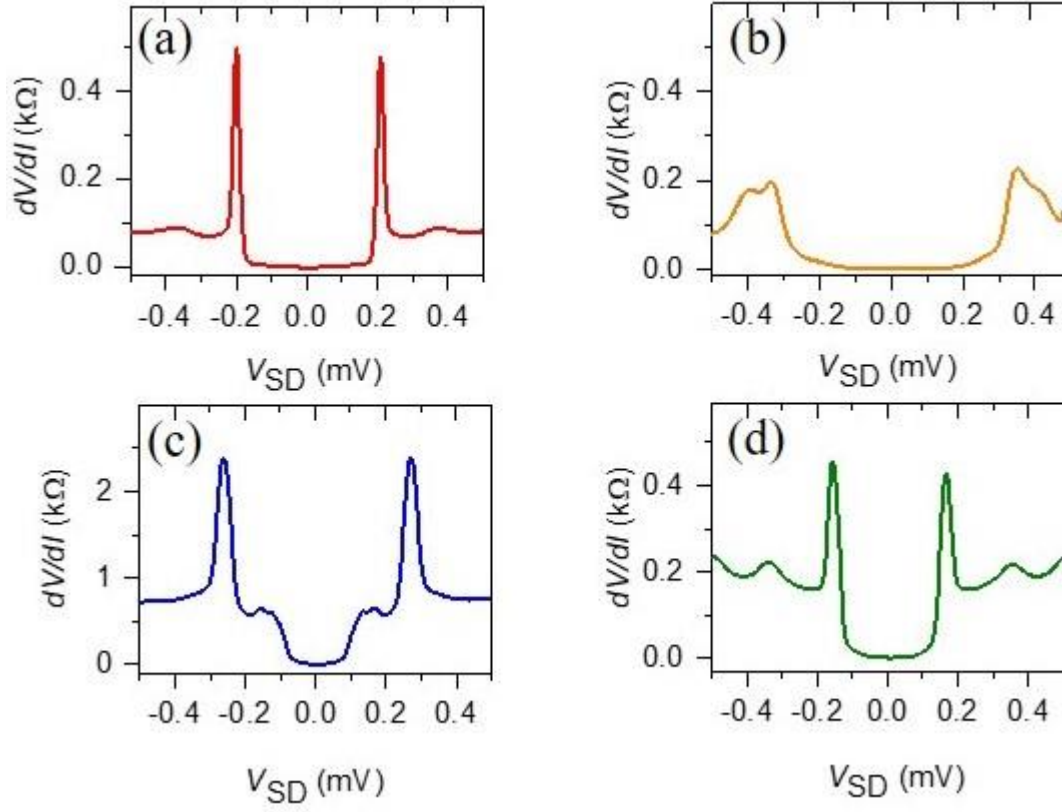


Figure S1. Induced superconducting properties in In_{0.75}Ga_{0.25}As quantum wells in D1-4. All curves are for base temperature $T=50$ mK.

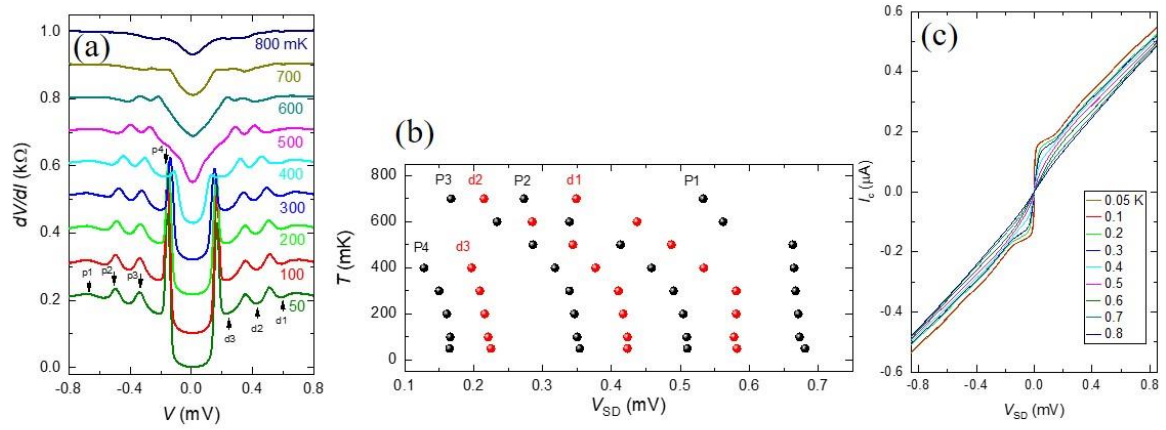


Figure S2. Temperature dependence induced superconducting gap with subharmonic-gap structures (SGS) oscillations due to multiple Andreev reflections observed in *D4*. The SGS and the induced gap peaks, are denoted by *P* while the dips are marked by *d*. (b) The SGS peaks and dips shown in (a) as a function of temperature and V_{SD} . (c) The current–voltage characteristics (*IVC*) curves as a function of temperature. The supercurrent in the Josephson junction is quite sensitive to temperature.

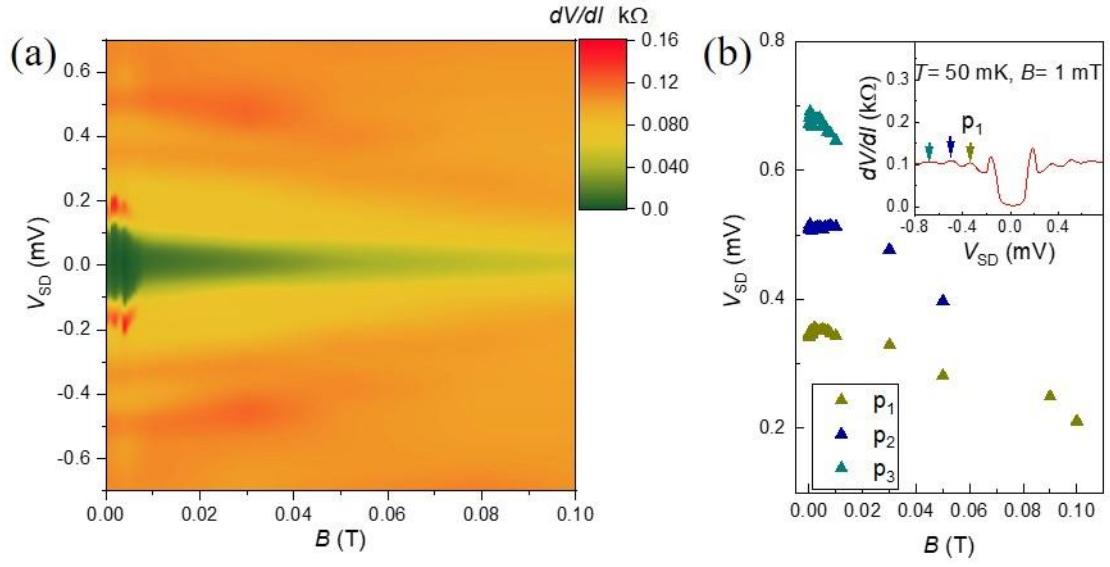


Figure S3. (a) Magnetic field dependence of induced superconductivity as a function of V_{SD} at temperature $T=50$ mK, in $D4$. (b) The dark yellow, blue, and dark cyan triangles (see their corresponding arrows in inset) indicate the magnetic field evolution of the induced- and SGS. Inset is the dV/dI (V) measured at $B_{\perp}=1$ mT and $T=50$ mK. Arrows correspond to SGS peaks.

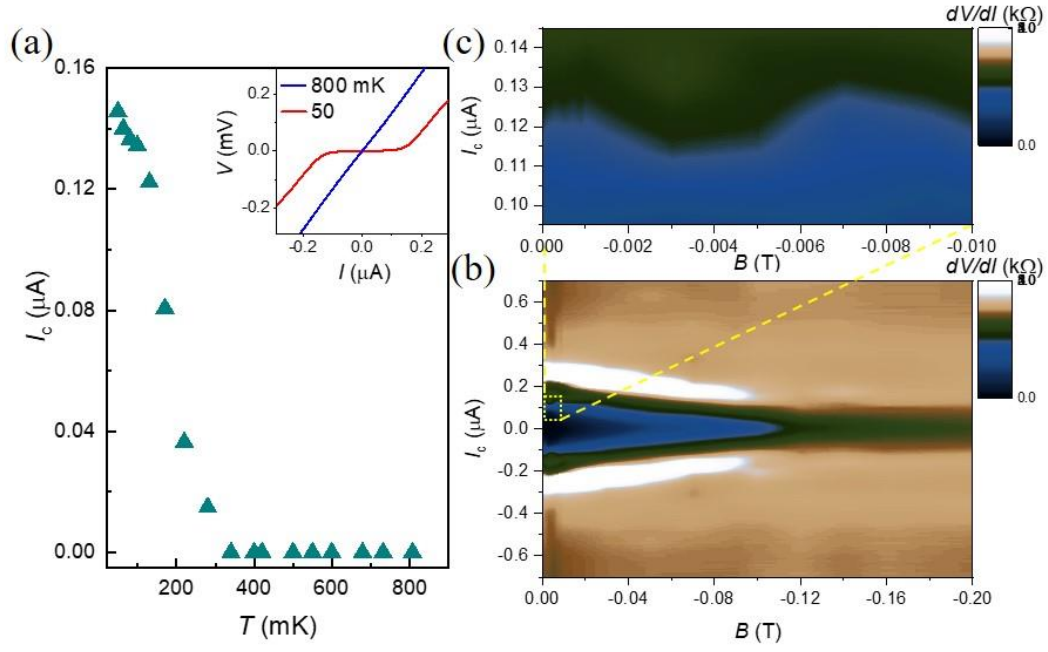


Figure S4. (a) The current–voltage characteristics (IVC) at $T = 50$ mK and 800 mK (inset) and the critical current I_c as a function of temperature for *D3*. (b) 2D plots of dV/dI as a function of I_c and B_\perp , at $T = 50$ mK. (c) 2D plots of dV/dI as a function of I_c and B_\perp shown for smaller magnetic field regions to highlight the supercurrent oscillation in the junction under application of the out-of-plane magnetic fields B_\perp .

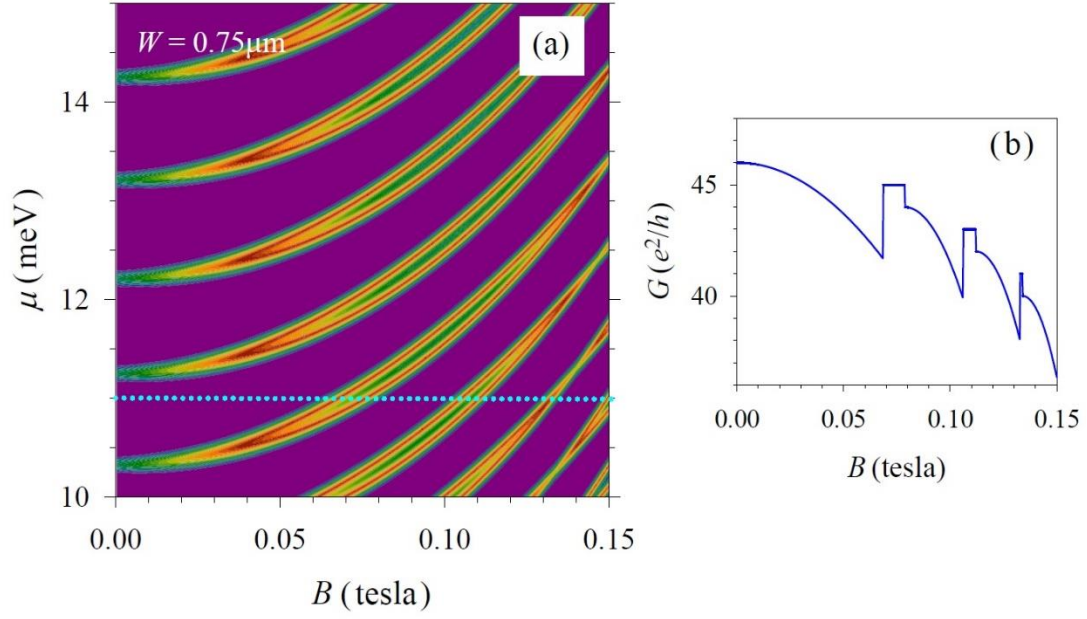


Figure S5. (a) Phase diagram of the hybrid 2DEG junction similar to Fig. 1b of the main text. The junction width is $w = 0.75 \mu\text{m}$ and the induced superconductivity is $\Delta_0 = 60 \mu\text{eV}$. (b) Theoretical conductance of the junction in the phenomenological model of our work along the sequence of magnetic fields of the line cut in panel (a). As explained in the main text, the model assumes a perfect Andreev reflection in the topological phases (plateaus), and a decreasing Andreev reflection AR (dips) with increasing field in the trivial phases due to interface scattering.

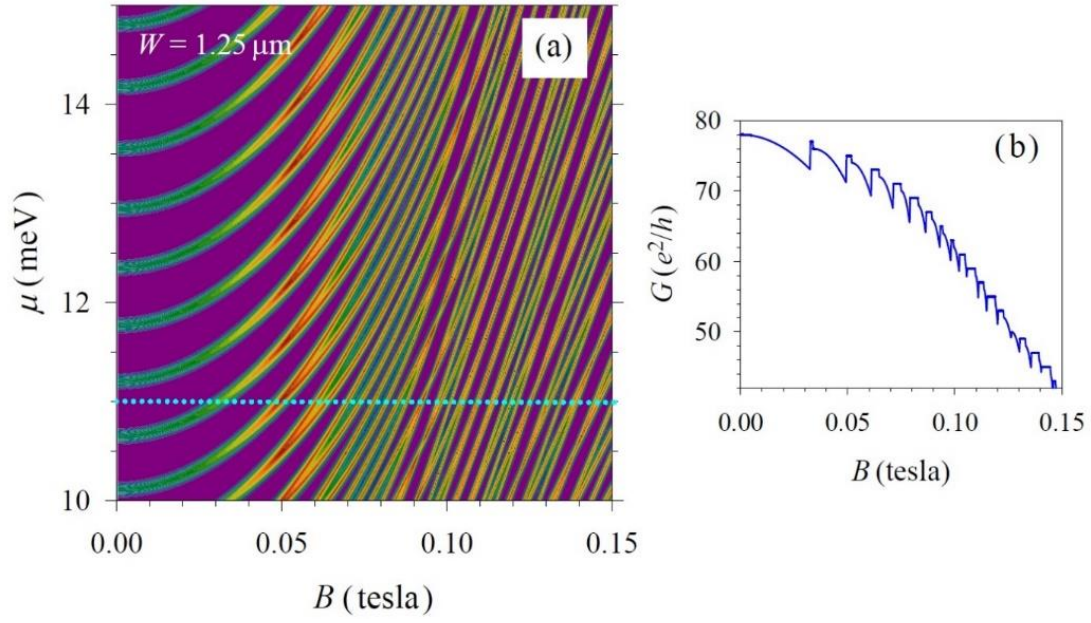


Figure S6. (a) Phase diagram of the hybrid 2DEG junction similar to Fig. 1b of the main text. The junction width is $w = 1.25 \mu\text{m}$ and the induced superconductivity is $\Delta_0 = 60 \mu\text{eV}$. (b) Theoretical conductance of the junction in the phenomenological model of our work along the sequence of magnetic fields of the line cut in panel (a). As explained in the main text, the model assumes a perfect Andreev reflection in the topological phases (plateaus), and a decreasing Andreev reflection AR (dips) with increasing field in the trivial phases due to interface scattering.

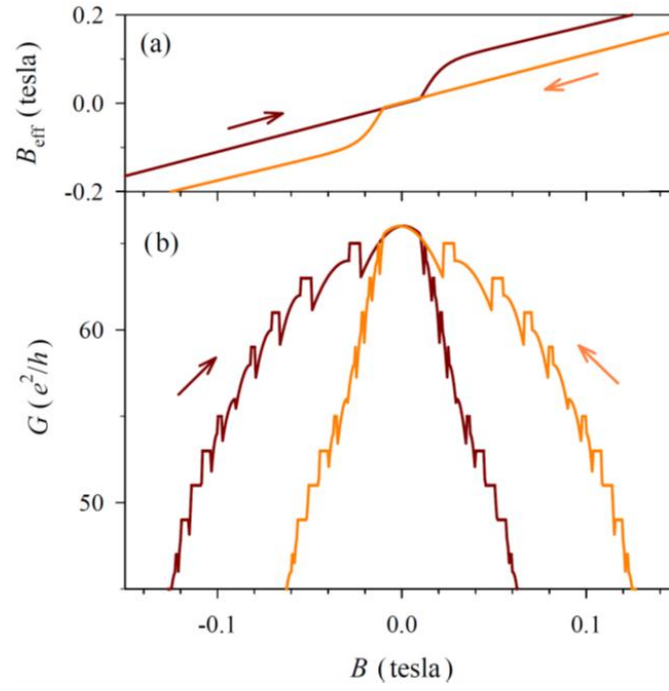


Figure S7. Numerical simulation of the magnetoconductance in topological Josephson junctions: (a) model of the hysteresis loop of the internal effective field B_{eff} when sweeping the external field B . The arrows indicate the sweep direction. (b) the modeled quantized conductance vs. applied out-of-plane magnetic field B_{\perp} in hybrid Josephson junction, explained in the text. The directions of external field B_{\perp} sweeps indicated by the arrows.